The Astrophysical Journal, 813:51 (14pp), 2015 November 1 doi:10.1088/0004-637X/813/1/51


# A MULTI-WAVELENGTH POLARIMETRIC STUDY OF THE BLAZAR CTA 102 DURING A GAMMA-RAY FLARE IN 2012

Carolina Casadio[1], José L. Gómez[1], Svetlana G. Jorstad[2,3], Alan P. Marscher[2], Valeri M. Larionov[3,4], Paul S. Smith[5], Mark A. Gurwell[6], Anne Lähteenmäki[4,7], Iván Agudo[1], Sol N. Molina[1], Vishal Bala[2], Manasvita Joshi[2], Brian Taylor[2], Karen E. Williamson[2], Arkady A. Arkharov[8], Dmitry A. Blinov[3,9], George A. Borman[10], Andrea Di Paola[11], Tatiana S. Grishina[3], Vladimir A. Hagen-Thorn[3], Ryosuke Itoh[12], Evgenia N. Kopatskaya[3], Elena G. Larionova[3], Liudmila V. Larionova[3], Daria A. Morozova[3], Elizaveta Rastorgueva-Foi[4,13], Sergey G. Sergeev[10], Merja Tornikoski[4], Ivan S. Troitsky[3], Clemens Thum[14], and Helmut Wiesemeyer[15]
[1] Instituto de Astrofísica de Andalucía, CSIC, Apartado 3004, E-18080 Granada, Spain
[2] Institute for Astrophysical Research, Boston University, 725 Commonwealth Avenue, Boston, MA 02215, USA
[3] Astronomical Institute, St. Petersburg State University, Universitetskij Pr. 28, Petrodvorets, 198504 St. Petersburg, Russia
[4] Aalto University Metsähovi Radio Observatory, Metsähovintie 114, FI-02540 Kylmälä, Finland
[5] Steward Observatory, University of Arizona, Tucson, AZ 85716, USA
[6] Harvard-Smithsonian Center for Astrophysics, Cambridge, MA 02138, USA
[7] Aalto University Department of Radio Science and Engineering, P.O. Box 13000, FI-00076 Aalto, Finland
[8] Pulkovo Observatory, St. Petersburg, Russia
[9] University of Crete, Heraklion, Greece
[10] Crimean Astrophysical Observatory, Nauchnij, Ukraine
[11] INAF, Osservatorio Astronomico di Roma, Roma, Italy
[12] Department of Physical Sciences, Hiroshima University, Higashi-Hiroshima, Hiroshima 739-8526, Japan
[13] School of Maths Physics, University of Tasmania, Private Bag 37, Hobart, TAS 7001, Australia
[14] Instituto de Radio Astronomía Milimétrica, Granada, Spain
[15] Max-Planck-Institut für Radioastronomie, Bonn, Germany
*Received 2015 July 27; accepted 2015 August 25; published 2015 October 28*

## ABSTRACT

We perform a multi-wavelength polarimetric study of the quasar CTA 102 during an extraordinarily bright $\gamma$-ray outburst detected by the *Fermi* Large Area Telescope in 2012 September–October when the source reached a flux of $F_{>100\,\mathrm{MeV}} = 5.2 \pm 0.4 \times 10^{-6}$ photons cm$^{-2}$ s$^{-1}$. At the same time, the source displayed an unprecedented optical and near-infrared (near-IR) outburst. We study the evolution of the parsec-scale jet with ultra-high angular resolution through a sequence of 80 total and polarized intensity Very Long Baseline Array images at 43 GHz, covering the observing period from 2007 June to 2014 June. We find that the $\gamma$-ray outburst is coincident with flares at all the other frequencies and is related to the passage of a new superluminal knot through the radio core. The powerful $\gamma$-ray emission is associated with a change in direction of the jet, which became oriented more closely to our line of sight ($\theta \sim 1\overset{\circ}{.}2$) during the ejection of the knot and the $\gamma$-ray outburst. During the flare, the optical polarized emission displays intra-day variability and a clear clockwise rotation of electric vector position angles (EVPAs), which we associate with the path followed by the knot as it moves along helical magnetic field lines, although a random walk of the EVPA caused by a turbulent magnetic field cannot be ruled out. We locate the $\gamma$-ray outburst a short distance downstream of the radio core, parsecs from the black hole. This suggests that synchrotron self-Compton scattering of NIR to ultraviolet photons is the probable mechanism for the $\gamma$-ray production.

*Key words:* galaxies: active – galaxies: jets – quasars: individual (CTA 102) – techniques: interferometric – techniques: photometric – techniques: polarimetric

*Supporting material:* machine-readable tables

## 1. INTRODUCTION

The Blazar CTA 102 (B2230+114) is classified as a highly polarized quasar, characterized by optical polarization exceeding 3% (Moore & Stockman 1981). Its high variability at optical wavelengths (Pica et al. 1988; Osterman Meyer et al. 2009) and its spectral properties also identify it as an optically violent variable quasar (Maraschi et al. 1986). Microvariability of CTA 102 at optical wavelengths has been investigated by Osterman Meyer et al. (2009), who found that faster variability is associated with higher flux states.

The variability in this source occurs at other frequencies as well: flares at centimeter and millimeter wavelengths have been registered in the past, as well as an X-ray flare detected by the *Rossi X-ray Timing Explorer* in late 2005 (Osterman Meyer et al. 2009). A radio flare in 1997 was related to the ejection of a new knot from the core (Savolainen et al. 2002; Rantakyrö et al. 2003; Jorstad et al. 2005), and another, in 2006, was connected with both the ejection of a new superluminal feature and the interaction between this component and a recollimation shock at 0.1 mas (Fromm et al. 2011).

The radio morphology on arcsecond scales (from images with the Very Large Array at 6 and 2 cm) reveals a central core with two weak components located at opposite sides (Spencer et al. 1989; Stanghellini et al. 1998). At higher angular resolution, CTA 102 has been regularly observed since 1995 within the Very Long Baseline Array (VLBA) 2 cm Survey (e.g., Zensus et al. 2002) and its successor, the MOJAVE program (e.g., Lister et al. 2009). MOJAVE images show that the jet in CTA 102 extends toward the southeast up to ∼15 mas

from the core, which corresponds to a de-projected distance of ∼2.7 kpc using the estimated viewing angle of 2°.6 obtained by Jorstad et al. (2005).

Kinematic studies of the MOJAVE data report apparent velocities between 1.39*c* and 8.64*c* (Lister et al. 2013). Higher apparent speeds, up to $\beta_{\rm app} \sim 18c$, have been reported in higher-resolution VLBA observations at 43 GHz by Jorstad et al. (2001, 2005). Apart from superluminal features, the jet of CTA 102 also displays standing features: two stationary components, A1 and C, have been observed at a distance of ∼0.1 and 2 mas from the core, respectively (Jorstad et al. 2001, 2005), and interpreted as recollimation shocks (Fromm et al. 2013b).

Recent MOJAVE polarimetric multifrequency observations (Hovatta et al. 2012) reveal a rotation measure gradient across the jet width at 7 mas from the core, which suggests the presence of a helical magnetic field in the jet. A similar result is reported in Fromm et al. (2013b), where the different observing frequencies reveal bends and helical structures in many parts of the jet.

CTA 102 was detected by the *Fermi Gamma-ray Space Telescope* in the first Large Area Telescope (LAT) catalog with a flux ($E > 100$ MeV) of $14.70 \pm 0.97 \times 10^{-8}$ photons cm$^{-2}$ s$^{-1}$ (Abdo et al. 2010a) and confirmed in the second catalog (Ackermann et al. 2011). In late 2012, the blazar exhibited an extraordinarily bright $\gamma$-ray outburst detected by the LAT, reaching a flux of $5.17 \pm 0.44 \times 10^{-6}$ photons cm$^{-2}$ s$^{-1}$ between 0.1 and 200 GeV. During the 2012 event, an unprecedented optical and near-infrared (near-IR) outburst was observed, as reported by Larionov et al. (2012) and Carrasco et al. (2012), respectively.

In this paper, we perform a radio to $\gamma$-ray multi-wavelength analysis in order to study the flaring activity of CTA 102 during the 2012 event. In Section 2, we present the multi-wavelength data set collected for the analysis, and we describe the methods used to reduce the data. In Section 3, we describe the characteristics of the emission at the different frequencies during the 2012 flare event. In Section 4, we study the kinematics and the flux density variability of the parsec scale jet. In Section 5, we perform the discrete cross-correlation analysis between light curves. In Section 6, we analyze the polarized emission of the source at millimeter and optical wavebands. We present our discussions and conclusions in Sections 7 and 8.

We adopt the cosmological values from the most recent *Planck* satellite results (Planck Collaboration et al. 2014): $\Omega_m = 0.3$, $\Omega_\Lambda = 0.7$, and $H_0 = 68$ km s$^{-1}$ Mpc$^{-1}$. With these values, at the redshift of CTA 102 ($z = 1.037$), 1 mas corresponds to a linear distance of 8.31 pc, and a proper motion of 1 mas yr$^{-1}$ corresponds to an apparent speed of 55.2*c*.

## 2. OBSERVATIONS AND DATA REDUCTION

We are interested in studying the multi-spectral behavior of CTA 102 during the $\gamma$-ray flare that occurred between 2012 September and October. For this, we have collected data from millimeter to $\gamma$-ray wavelengths, extending our study from 2004 June to 2014 June. In particular, the *Fermi* data extend from the start of the mission (2008 August) to 2013 September, X-ray and UV data cover the observing period from 2009 August to 2013 June, optical and NIR data from 2004 June to 2013 October, and the combined radio light curves cover the entire period from 2004 June to 2014 June.

In the millimeter-wave range, we use data at (1) 350 GHz (0.85 mm) and 230 GHz (1.3 mm), obtained with the Submillimeter Array (SMA) at Mauna Kea, Hawaii; (2) 230 GHz (1.3 mm) and 86.24 GHz (3.5 mm) with the 30 m Telescope of Institut de Radioastronomie Millimétrique (IRAM) at the Pico Veleta Observatory (Spain); (3) 43 GHz (7 mm) with the VLBA; and (5) 37 GHz (8 mm) with the 13.7 m Telescope at Metsähovi Radio Observatory of Aalto University (Finland).

NIR photometric data (JHK filters) were obtained at the Perkins Telescope at Lowell Observatory (Flagstaff, AZ) using the MIMIR instrument (Clemens et al. 2007) and at the 1.1 m Telescope of the Main Astronomical Observatory of the Russian Academy of Sciences located at Campo Imperatore, Italy (see Hagen-Thorn et al. 2008 for details).

We have collected optical photometric data in the *UBVRI* bands from numerous telescopes: (1) the 2.2 m Telescope of Calar Alto Observatory (Almería, Spain)[16]; (2) the 2 m Liverpool Telescope of the Observatorio del Roque de Los Muchachos (Canary Island, Spain); (3) the 1.83 m Perkins Telescope of Lowell Observatory (Flagstaff, AZ); (4) the 1.54 m and 2.3 m telescopes of Steward Observatory (Mt. Bigelow and Kitt Peak, AZ)[17]; (5) the 40 cm LX-200 Telescope of St. Petersburg State University (St. Petersburg, Russia); (6) the 70 cm AZT-8 Telescope of the Crimean Astrophysical Observatory (Nauchnij, Ukraine); (7) the 1.5 m Kanata Telescope in Higashi-Hiroshima Observatory (Japan)[18]; and (8) the Ultraviolet and Optical Telescope (UVOT) on board the *Swift* satellite. Optical data are in part also in polarimetric mode, mostly in the *R* band, except for items (4) and (5) listed above (see Schmidt et al. 1992; Hagen-Thorn et al. 2008, respectively, for details). In the UV range, we use UVOT data from *Swift* in the three available filters: UVW2 (2030 Å), UVM2 (2231 Å), and UVW1 (2634 Å). We have also obtained X-ray data in the energy range 0.3–10 keV from the X-ray Telescope on board the *Swift* satellite.

At the highest photon energies considered here, we have analyzed $\gamma$-ray data from the LAT of the *Fermi Gamma-ray Space Telescope*.

### 2.1. $\gamma$-Ray Data Analysis

We have analyzed the $\gamma$-ray data of the field containing CTA 102 from *Fermi* LAT from 2008 August to 2013 September, producing a light curve between 0.1 and 200 GeV with an integration time of 1 day. We used the *Fermi* Science Tools version v9r33p0 and instrument response function P7REP_SOURCE_V15, considering data inside a region of interest (ROI) of 15° radius centered on CTA 102. We followed the unbinned likelihood procedure as described at http://fermi.gsfc.nasa.gov/ssc/data/analysis/scitools/.

The procedure starts with the selection of good data and time intervals through the tasks *gtselect* and *gtmktime* and follows with the creation of an exposure map for each day (tasks *gtltcube*, *gtexpmap*) and the modeling of data through a maximum-likelihood method (*gtlike*). In this last step, we used a model that includes CTA 102 and 42 other point sources inside the ROI, according to the second *Fermi* Gamma-ray Catalog (2FGL; Ackermann et al. 2011). The model also takes

[16] Observations performed under MAPCAT (Monitoring AGN with the Calar Alto Telescopes); see Agudo et al. (2012).
[17] Data taken from the Steward Observatory monitoring project; see Smith et al. (2009).
[18] Data published in Itoh et al. (2013).

into account the diffuse emission from our Galaxy (*gll_iem_v05.fit*) and the extragalactic $\gamma$-ray background (*iso_source_v05.txt*). We searched for the flux normalization of CTA 102 by fixing the spectral index of the other point sources while varying both the flux and spectral index of our target. The $\gamma$-ray spectrum of CTA 102 was modeled with a log parabola curve corresponding to the spectral model given in the 2FGL catalog. We considered a successful detection when the test statistic TS $\geqslant$ 10, which corresponds to a signal-to-noise ratio $\gtrsim 3\sigma$ (Nolan et al. 2012).

### 2.2. X-ray, UV, Optical, and NIR

We collected X-ray and UV data from 2009 August to 2013 June from the *Swift* archive. The X-ray data in the energy range 0.3–10 keV were calibrated following the procedure described in Williamson et al. (2014). The UVOT data reduction was performed via the UVOTSOURCE tool, with a sigma value of 5 adopted to compute the background limit. Optical and NIR data were reduced and calibrated following the procedures outlined in Jorstad et al. (2010).

All of the magnitudes of the optical and NIR data have been corrected for Galactic extinction with values reported in the NASA Extragalactic Database[19] for each filter (Schlafly & Finkbeiner 2011). For the UV data, we obtained the absolute extinction value at each wavelength $A(\lambda)$ from Equation (1) in Cardelli et al. (1989). After the correction, we transformed magnitudes into fluxes using the formula reported in Mead et al. (1990) and Poole et al. (2008).

### 2.3. Photopolarimetric Millimeter VLBA and Single-dish Data

Multi-epoch very long baseline interferometer (VLBI) images provide ultra-high angular resolution that can be used to determine the location in the jet where flaring activity occurs. We therefore have collected data from the VLBA-BU-BLAZAR program,[20] which consists of monthly monitoring of $\gamma$-ray bright blazars with the VLBA at 43 GHz (7 mm). The data set consists of 80 total and polarized intensity images from 2007 June to 2014 June. We restore the images with a common convolving beam of 0.4 $\times$ 0.2 milliarcseconds (mas). Since the resolution of the longest baselines of the VLBA is less than half of these dimensions, we employ model fitting to define and determine the parameters of the very fine-scale structure. The data reduction was performed with a combination of the Astronomical Image Processing System (`AIPS`) and the Differential Mapping software (`Difmap`), as described in Jorstad et al. (2005). The electric vector position angle (EVPA) calibration follows the procedure discussed in Jorstad et al. (2005), which combines the comparison between VLA and VLBA integrated EVPA values at those epochs for which VLA data are available with the method of Gómez et al. (2002) that utilizes the stability of the instrumental polarization (D-terms).

The IRAM 30 m Telescope's total flux and polarimetric data in this paper were acquired under the POLAMI (Polarimetric AGN Monitoring at the IRAM 30 m Telescope) program (see I. Agudo et al. 2015, in preparation) and reduced and calibrated following the procedures introduced in Agudo et al. (2006, 2010, 2014).

[19] http://ned.ipac.caltech.edu/

[20] http://www.bu.edu/blazars/research.html

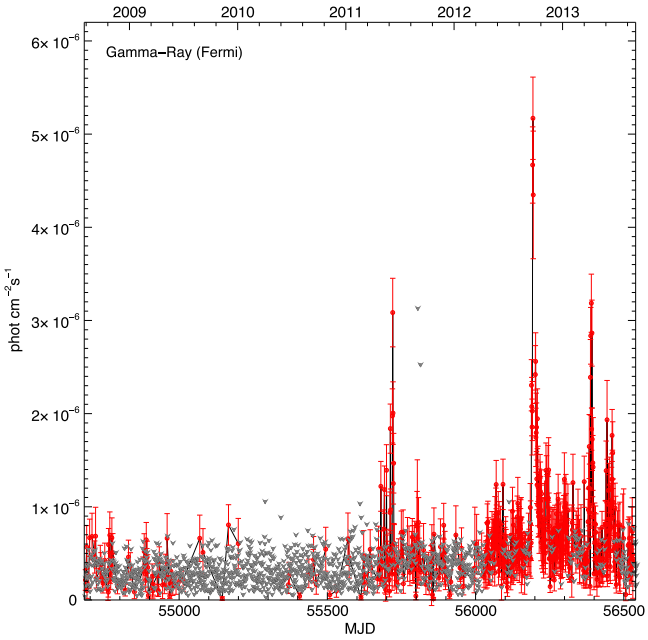


**Figure 1.** *Fermi* LAT $\gamma$-ray light curve between 0.1 and 200 GeV, with an integration time of 1 day. Red points represent the detections (TS $>$ 10), and gray arrows correspond to upper limits when the source is not detected (TS $<$ 10).

The Submillimeter Array data of CTA 102 came from an ongoing monitoring program at the SMA to determine the fluxes of compact extragalactic radio sources that can be used as calibrators at millimeter wavelengths (Gurwell et al. 2007). Observations of available potential calibrators are from time to time observed for 3–5 minutes, and the measured source signal strength are calibrated against known standards, typically solar system objects (Titan, Uranus, Neptune, or Callisto). Data from this program are updated regularly and are available at the SMA website.[21]

## 3. MULTI-WAVELENGTH OUTBURST

Figure 1 displays the $\gamma$-ray light curve of CTA 102 in the energy range 0.1–200 GeV during the period of major activity (2011 June–2013 April) obtained with an integration time of 1 day. Following Jorstad et al. (2013), we can define a $\gamma$-ray outburst as a period when the flux exceeds a threshold of $2 \times 10^{-6}$ photons cm$^{-2}$ s$^{-1}$. Although this is an arbitrary limit, it conforms to a visual inspection of the $\gamma$-ray light curve of CTA 102.

The first outburst takes place in 2011 June (MJD 55719–55721), when the source displays a one-day peak flux of $3.1 \pm 0.37 \times 10^{-6}$ photons cm$^{-2}$ s$^{-1}$. The second, brightest outburst occurs at the end of 2012 September (2012.73), when the source remains above $2 \times 10^{-6}$ photon cm$^{-2}$ s$^{-1}$ for 14 days (from MJD 56188 to 56202), reaching a peak of $5.2 \pm 0.4 \times 10^{-6}$ photons cm$^{-2}$ s$^{-1}$ on MJD 56193. During this outburst, the $\gamma$-ray flux increases by a factor of 10 in just 6 days. The third flare occurs in 2013 April (MJD 56387–56394) and lasts 8 days. On this occasion (MJD 56392), the blazar reaches a peak of $2.9 \pm 0.4 \times 10^{-6}$ photons cm$^{-2}$ s$^{-1}$.

We compare the daily $\gamma$-ray light curve with the X-ray, UV, optical, NIR, and radio light curves in Figure 2. Table 1 lists

[21] http://sma1.sma.hawaii.edu/callist/callist.html

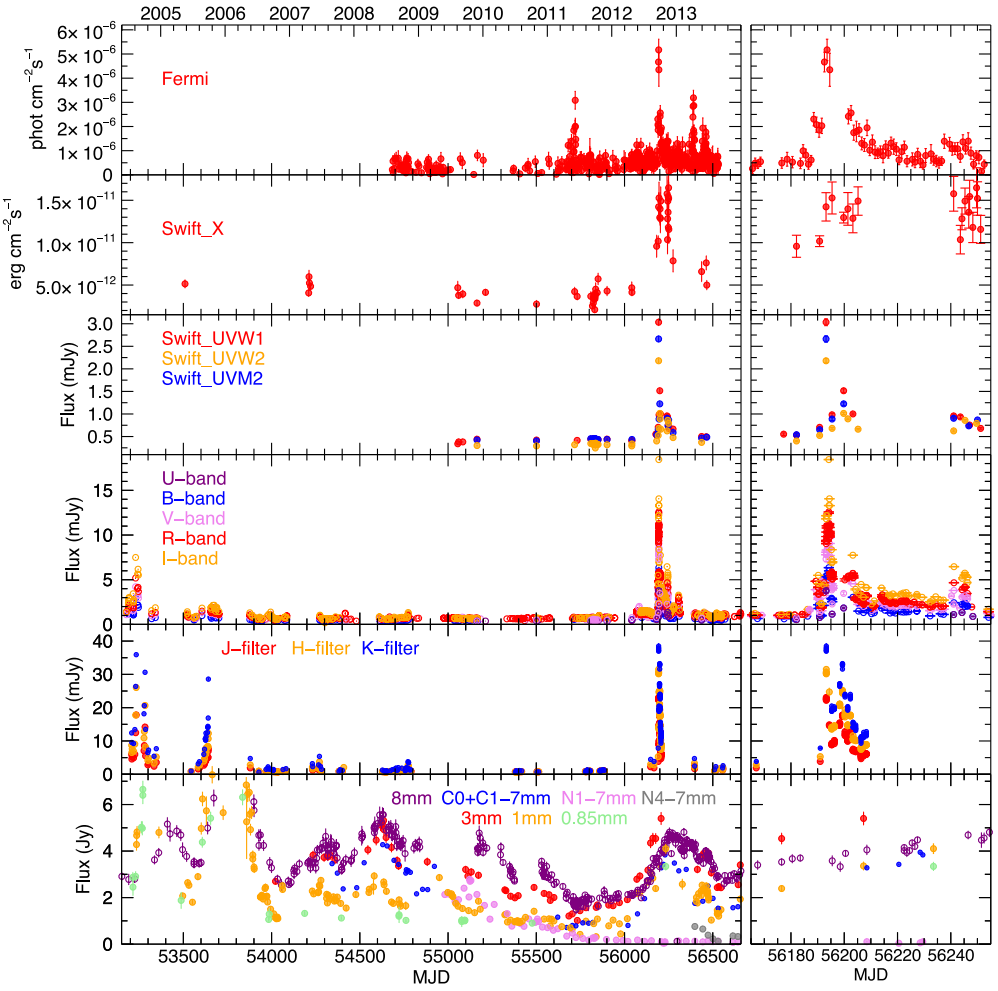


**Figure 2.** Light curves of CTA 102 from γ-ray to millimeter wavelengths. From top to bottom: γ-ray, X-ray, UV, optical, NIR, and millimeter-wave data. Left panel: data from 2004 May to 2014 January. Right panel: expanded view during the γ-ray outburst between 2012 August and November.

**Table 1**
Multi Wavelength Data

| γ-Ray Data | Flux | Energy Band |
|---|---|---|
| Epoch (MJD) | (photons cm$^{-2}$ s$^{-1}$) | (GeV) |
| 54684.2 | 2.15e-07 ± 1.11e-07 | 0.1–200 |
| 54688.2 | 5.68e-07 ± 2.30e-07 | 0.1–200 |
| 54689.2 | 10.00e-08 ± 8.30e-08 | 0.1–200 |
| X-ray data | | |
| Epoch (MJD) | Flux (photons cm$^{-2}$ s$^{-1}$) | Energy Band (KeV) |
| 53509.4 | 5.14e-12 ± 4.74e-13 | 0.3–10 |
| 54210.2 | 4.07e-12 ± 4.13e-13 | 0.3–10 |
| 54212.1 | 5.97e-12 ± 7.67e-13 | 0.3–10 |

(This table is available in its entirety in machine-readable form.)

the multi-wavelength data used in our analysis. The brightest γ-ray outburst, in 2012 September, is accompanied by similarly bright flares at all of the other wavebands. This is, however, not the case for the other two orphan γ-ray flares (γ-ray outbursts with no correspondence at any of the other observing bands), with the exception of a millimeter-wave flare that follows the third γ-ray flare in 2013 April.

Analyzing the multi-wavelength flare in 2012, we observe that the X-ray light curve contains a double-peak structure, where the first peak is almost coincident with the γ-ray outburst and the second peak occurs ∼50 days later. The limited sampling of the X-rays prevents a deeper analysis of the overall X-ray behavior associated with this flare. The UV and optical bands exhibit a rapid and pronounced increase in the light curves coinciding with the γ-ray flare. In the optical light curve, we distinguish a secondary, weaker flare after ∼50 days, close to the second X-ray peak, as well as a third, smaller outburst that occurs ∼70 days after the second peak. In the UV it is also possible to distinguish a secondary flare delayed by ∼50 days with respect to the main flare, but the sampling of the data is insufficient to specify the behavior in more detail. In the NIR light curve, we observe a large flare coincident with the γ-ray flare, but there is no further sampling after this. A detailed analysis of the NIR flare shown in Figure 3 reveals that the event consists of three sub-flares covering almost the entire period of high γ-ray flux from MJD 56193 to 56202.

The radio light curve also exhibits an increase in flux density during the 2012 γ-ray outburst, but with a much longer timescale, lasting ∼200 days. The 1 mm light curve and 7 mm light curves of features C0 and C1 peak on ∼MJD 56230,

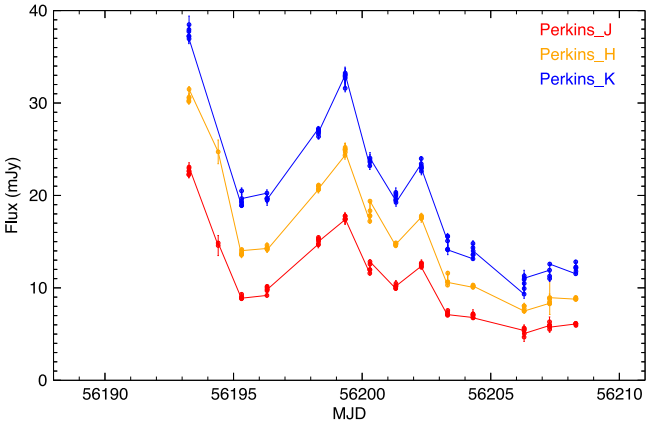


**Figure 3.** Expanded view of the NIR light curve in the *J*, *H*, and *K* bands during the period of the main $\gamma$-ray outburst.

about 1 month after the $\gamma$-ray flare. The 3 mm light curve follows a similar trend, starting to increase on ∼MJD 56000. Our limited time sampling between MJD 56208 and 56412 shows a peak on MJD 56207, very close to the $\gamma$-ray flare, although we cannot rule out the possibility that the actual peak is closer to that at 1 mm.

## 4. THE PARSEC-SCALE JET

### 4.1. Physical Parameters of Components

VLBA images of CTA 102 at some selected epochs are displayed in Figures 4–6. To carry out an analysis of the jet kinematics and flux density variability, we have fit with `Difmap` the complex visibilities with a model source consisting of components described by circular Gaussian brightness distributions. For each epoch, we obtained a model fit that provides information about the flux density ($S$), distance ($r$), and position angle ($\Theta$) relative to the core and the FWHM size ($a$) of each component. The core (labeled C0), considered stationary over the entire period, is identified with the unresolved component in the northwestern (upstream) end of the jet. It is the brightest feature in the jet at most of the epochs. Polarization information has been obtained with an IDL program that calculates the mean values of the degree of polarization ($m$) and EVPA ($\chi$) over the image area defined by the FWHM size of each component. The uncertainties of both $m$ and $\chi$ correspond to the standard deviations of their respective distributions. Model-fit parameters for all components and epochs are reported in Table 2.

The accuracy of the model-fit parameters for each component depends on its brightness temperature, so that smaller uncertainties are expected for more compact components and higher flux densities. We have therefore established a criterion for quantifying the errors in the model-fit parameters that is directly related to the observed brightness temperature, $T_{\rm b} = 7.5 \times 10^8\ S/a^2$ (e.g., Jorstad et al. 2005), where $T_{\rm b}$ is measured in Kelvins (K), $S$ in Janskys (Jy), and $a$ in milliarcseconds (mas).

First, we select a representative sample of epochs and components with a wide range of $S$, $a$, and $r$ values. For each one of these components, we compute the error in the fitted parameters by analyzing how the reduced $\chi^2$ of the fit and resulting residual map change when varying the fitted parameters one at a time. We set a limit on the maximum allowed variation of the reduced $\chi^2$ of 20%, corresponding to an increase by a factor of ∼1.5 in the peak levels of the residual map. According to this criterion, we assign a series of uncertainties in position and flux density to the components in the sample. We then relate the derived uncertainties with the measured brightness temperature, obtaining the following relations:

$$\sigma_{xy} \approx 1.3 \times 10^4\ T_{\rm b}^{-0.6}, \quad (1)$$

$$\sigma_S \approx 0.09\ T_{\rm b}^{-0.1}, \quad (2)$$

where $\sigma_{xy}$ and $\sigma_S$ are the uncertainties in the position (R.A. or decl.) and flux density, respectively. These relations have been used to compute the errors in the position and flux density for all of the fitted components. To account for the errors in the flux calibration, we have added in quadrature a 5% error to the uncertainty in flux density. The uncertainties in the sizes of components are also expected to depend on their brightness temperatures. Following Jorstad et al. (2005), we have assigned a 5% error to the sizes of the majority of components (those with flux densities $\geqslant$50 mJy and sizes of 0.1–0.3 mas) and a 10% error for more diffuse components.

Plots of separation and flux density versus time for the model-fit jet components, including the core, are presented in Figures 7 and 8. Besides the core, we have identified seven main components that could be traced reliably across multiple epochs. Component E1, located at ∼2 mas from the core, is a weak and extended feature that appears to be quasi-stationary across some epochs, or to move with a significantly slower velocity than other moving components (see Figure 7). A stronger and more compact component, C1, can be distinguished from the core at most of the observed epochs, located at a mean distance of $r \sim 0.1$ mas. Both quasi-stationary features have been observed previously by Jorstad et al. (2005) and Fromm et al. (2013a, 2013b) and interpreted as recollimation shocks in the jet. We identify five other moving components, N1, N2, N3, N4, and S1. Component S1 seems, however, to have a different nature: it appears to form in the wake of component N1 at a distance of ∼0.5 mas, and it is observed over only four epochs afterward. Its properties are similar to those expected and observed previously for trailing components (Agudo et al. 2001; Gómez et al. 2001; Jorstad et al. 2005). Linear fits of separation versus time have been obtained for the other moving components, N1, N2, N3, and N4, based on only those initial epochs at which an accurate position is obtained (see also Figure 7). This yields the estimates for the apparent velocities and times of ejection (epoch at which the component coincides with the core) listed in Table 3.

Since we cannot directly measure the radial velocities of the jet features, a common approach to disentangle the contributions of the component's Lorentz factor and viewing angle in the observed proper motion is the use of the flux variability (e.g., Jorstad et al. 2005; Hovatta et al. 2009). Following Jorstad et al. (2005), we use causality arguments to infer the variability Doppler factor

$$\delta_{\rm var} = \frac{s D_{\rm L}}{c \triangle t_{\rm var} (1+z)}, \quad (3)$$

where $s$ is the disk-equivalent angular diameter (where $s = 1.6a$ for a Gaussian component fit with FWHM $= a$ measured at the

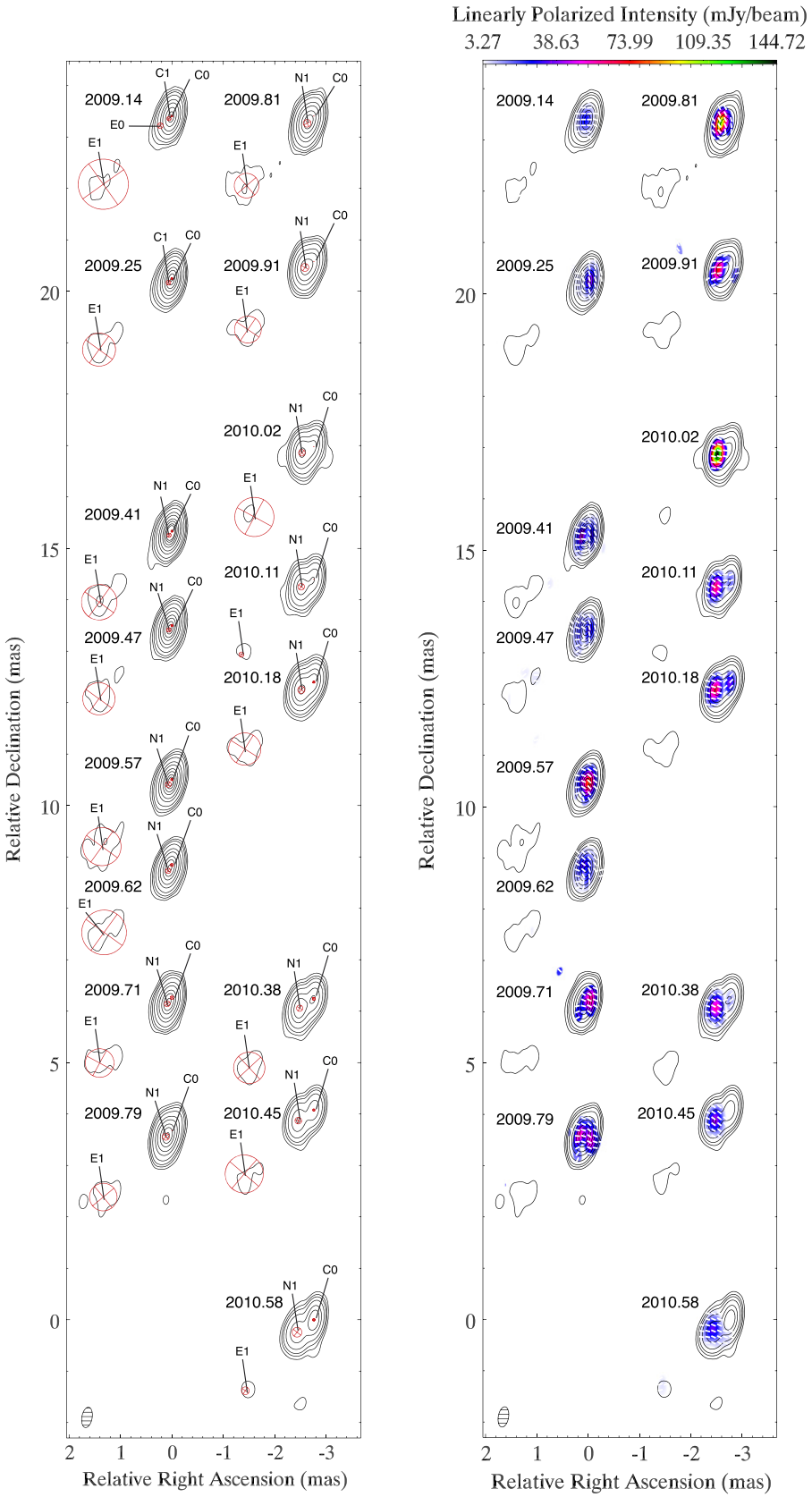


**Figure 4.** Sequence of 43 GHz VLBA images displaying epochs from 2009 February to 2010 August, when we observe the appearance of component N1. The images are restored with a common beam of 0.4 × 0.2 mas at −10° and are separated by a distance proportional to the time elapsed between observing epochs. Left panel: contours (total intensity) are traced at 0.003, 0.008, 0.04, 0.1, 0.3, 0.6, 1.2, 1.8, 2.5, and 3.0 Jy beam$^{-1}$ and $I_{\rm peak}$ = 4.2 Jy beam$^{-1}$. Red circles represent model-fit components. Right panel: same contours (total intensity) as in the left panel plus colors that represent linearly polarized intensity and white sticks symbolizing linear polarization angle.

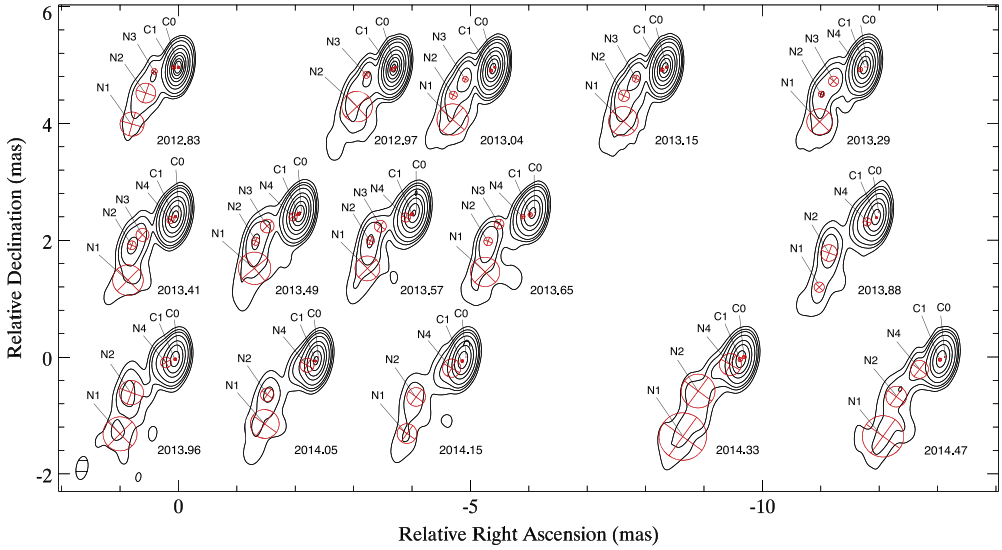


**Figure 5.** Sequence of total intensity 43 GHz VLBA images from 2012 October to 2014 June, covering the epochs from which we start observing component N4. Peak intensity is $I_{\rm peak} = 3.6$ Jy beam$^{-1}$ and contours are traced at 0.003, 0.008, 0.04, 0.1, 0.3, 0.6, 1.2, 1.8, 2.5, and 3.0 Jy beam$^{-1}$.

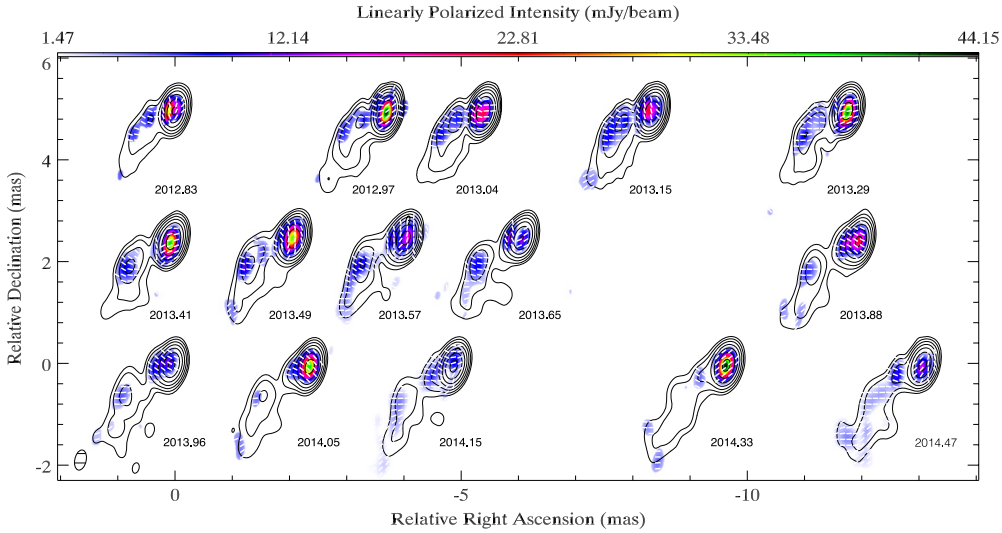


**Figure 6.** Same as Figure 5, but with linearly polarized intensity in colors and white sticks symbolizing linear polarization angle.

epoch of maximum flux), and $D_{\rm L}$ is the luminosity distance. The variability timescale is defined as $\Delta t_{\rm var} = dt/\ln(S_{\rm max}/S_{\rm min})$, where $S_{\rm max}$ and $S_{\rm min}$ are the measured maximum and minimum flux densities, respectively, and $dt$ is the time in years between $S_{\rm max}$ and $S_{\rm min}$ (Burbidge et al. 1974). This definition of $\delta_{\rm var}$ is valid under the assumption that the flux density variability timescale corresponds to the light-travel time across the component, which is valid as long as the radiative cooling time is shorter than the light crossing time and expansion time. Combining the estimated value of $\delta_{\rm var}$ with the measured apparent velocity, $\beta_{\rm app} = \beta \sin\theta/(1 - \beta\cos\theta)$, where $\theta$ and $\beta$ are the viewing angle and velocity (in units of the speed of light) of the component, we can calculate the variability Lorentz factor, $\Gamma_{\rm var}$, and viewing angle, $\theta_{\rm var}$, using (Hovatta et al. 2009)

$$\Gamma_{\rm var} = \frac{\beta_{\rm app}^2 + \delta_{\rm var}^2 + 1}{2\delta_{\rm var}} \quad (4)$$

and

$$\theta_{\rm var} = \arctan\frac{2\beta_{\rm app}}{\beta_{\rm app}^2 + \delta_{\rm var}^2 - 1}. \quad (5)$$

Physical parameters of the moving components obtained from this method are reported in Table 4.

### 4.2. Kinematics and Flux Density Variability

By inspecting the light curves in Figure 8, we can identify two flaring periods in the core: a prolonged first event that extends from mid-2007 to the beginning of 2009, and a second one between mid-2012 and the beginning of 2013, in coincidence with the main $\gamma$-ray flare.

The peak flux of the first flare occurs between 2008 June and July, when both components C0 and C1 increase their flux densities, reaching a combined value of $\sim$4.2 Jy. Due to the proximity of C1 to the core, it is not always possible for the model-fitting routine to clearly distinguish the two components, leading to high uncertainties in the flux ratio of the two

**Table 2**
VLBA 43 GHz Model-fit Components' Parameters

| Epoch (year) | Epoch (MJD) | Flux (mJy) | Distance from C0 (mas) | Pos. Angle (°) | Major Axis (mas) | Degree of Polarization (%) | EVPAs (°) |
|---|---|---|---|---|---|---|---|
| | | | Component C0 | | | | |
| 2007.45 | 54264.5 | 3086 ± 313 | ... | ... | 0.017 ± 0.001 | ... | ... |
| 2007.53 | 54294.5 | 3423 ± 347 | ... | ... | 0.034 ± 0.002 | 1.5 ± 0.2 | 71.2 ± 5.7 |
| 2007.59 | 54318.5 | 2340 ± 239 | ... | ... | 0.038 ± 0.002 | 2.4 ± 0.1 | 76.4 ± 5.4 |
| 2007.66 | 54342.5 | 3163 ± 321 | ... | ... | 0.045 ± 0.002 | 1.6 ± 0.1 | 71.9 ± 6.6 |
| 2007.74 | 54372.5 | 2743 ± 279 | ... | ... | 0.045 ± 0.002 | 1.4 ± 0.1 | 82.9 ± 8.4 |
| | | | Component C1 | | | | |
| 2007.66 | 54342.5 | 296 ± 37 | 0.07 ± 0.01 | 119.2 ± 3.2 | 0.062 ± 0.003 | 1.6 ± 0.1 | 65.5 ± 7.1 |
| 2007.74 | 54372.5 | 307 ± 37 | 0.09 ± 0.01 | 104.4 ± 4.8 | 0.031 ± 0.002 | 2.2 ± 0.1 | −80.8 ± 6.3 |
| 2007.83 | 54405.5 | 168 ± 25 | 0.13 ± 0.02 | 119.5 ± 3.2 | 0.116 ± 0.006 | 2.6 ± 0.2 | 79.3 ± 5.9 |
| 2008.04 | 54482.5 | 575 ± 64 | 0.08 ± 0.01 | 146.2 ± 1.9 | 0.070 ± 0.003 | 0.7 ± 0.1 | 37.8 ± 5.5 |
| 2008.16 | 54524.5 | 894 ± 96 | 0.09 ± 0.01 | −166.3 ± 7.4 | 0.062 ± 0.003 | 0.5 ± 0.1 | 38.2 ± 5.6 |

(This table is available in its entirety in machine-readable form.)

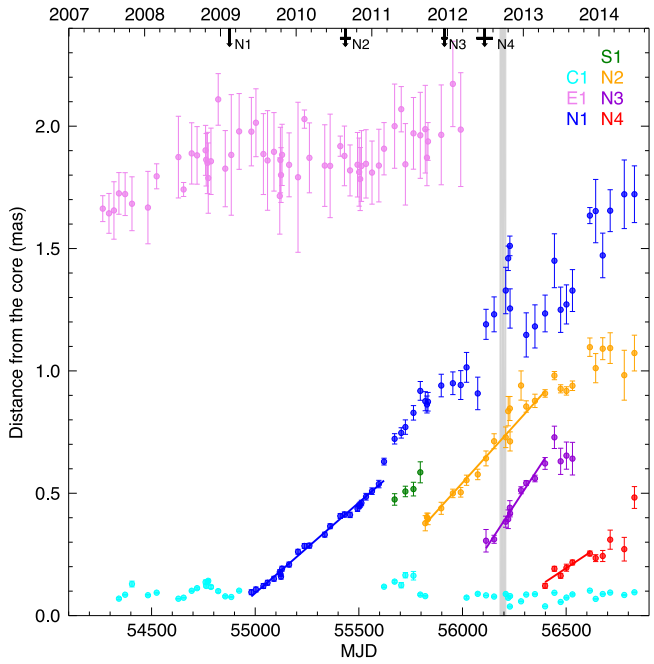


**Figure 7.** Distance from the core vs. time for the 43 GHz model-fit components, with linear fits overlaid. Downward black arrows mark the time of ejection of each component with the respective error bar. The gray vertical stripe indicates the epoch of the $\gamma$-ray flare.

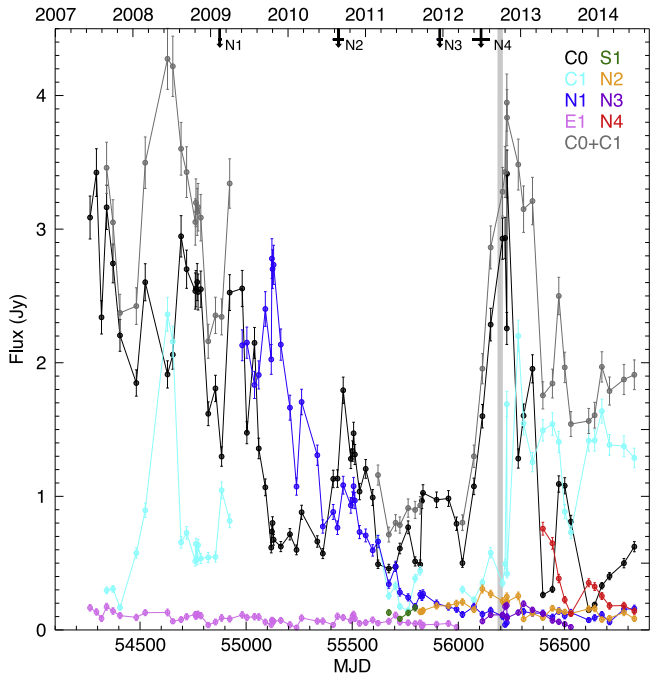


**Figure 8.** Light curves of 43 GHz model-fit components. Downward arrows and the gray vertical stripe indicate the same as in Figure 7.

features, as well as uncertainties in the position of C1. Because of this, Figure 8 also shows the combined flux density of the core and component C1, providing the data needed to follow the total flux density within the core region of CTA 102.

The second flare in the millimeter-wave core began in mid-2012, reaching its peak flux density at the end of 2012 October, close to the $\gamma$-ray flare (see Figure 8; Section 5). After the peak, the core region (C0 plus C1) remains in a high flux state until the last observing epoch, with a combined flux density oscillating around ∼2 Jy.

Both flares in the core region are associated with the appearance of subsequent superluminal components. In the case of the first such flare, component N1 appears as a bright and well-defined feature that moves along the jet at 14.9 ± 0.2 $c$ (see Figures 7–8 and Table 3). We also note that the ejection of component N1 corresponds to a change in the innermost structure of the compact jet, after which component C1 is no

**Table 3**
Kinematics of Moving Jet Features

| Name | N.Epoch | $\mu$ (mas yr$^{-1}$) | $\beta_{\rm app}$ ($c$) | $T_{ej}$ (year) |
|---|---|---|---|---|
| N1 | 26 | 0.27 ± 0.01 | 14.9 ± 0.2 | 2009.12 ± 0.02 |
| N2 | 18 | 0.35 ± 0.01 | 19.4 ± 0.8 | 2010.65 ± 0.07 |
| N3 | 10 | 0.49 ± 0.03 | 26.9 ± 1.8 | 2011.96 ± 0.07 |
| N4 | 6 | 0.21 ± 0.02 | 11.3 ± 1.2 | 2012.49 ± 0.11 |

**Table 4**
Physical Parameters of Moving Jet Features

| Name | $\triangle t_{\rm var}$ (year) | $a_{\rm max}$[a] (mas) | $\delta_{\rm var}$ | $\theta_{\rm var}$ (°) | $\Gamma_{\rm var}$ |
|---|---|---|---|---|---|
| N1 | 0.70 | 0.14 | 14.6 | 3.9 | 14.9 |
| N2 | 1.12 | 0.33 | 22.4 | 2.5 | 19.6 |
| N3 | 0.28 | 0.09 | 26.1 | 2.2 | 26.2 |
| N4 | 0.20 | 0.08 | 30.3 | 1.2 | 17.3 |

**Note.**
[a] FWHM of the model-fit component calculated at the epoch of maximum flux.

longer detected for almost two years. The second core flare leads to the ejection of component N4, which is significantly weaker than component N1 and has the slowest proper motion of the analyzed components (see Figures 7–8 and Table 3).

The values of the variability Doppler factors listed in Table 4 correspond to a progressive increase with time, from 14.6 for component N1 to 30.3 for component N4. Previous estimations of the variability Doppler factor in CTA 102 range between 15.6 (Hovatta et al. 2009) and 22.3 ± 4.5 (Jorstad et al. 2005), making N4 the superluminal knot with the highest Doppler factor to date. According to our analysis, this unusually large value is due to a progressive re-orientation in the direction of ejection of knots, from $\theta_{\rm var} = 3\overset{\circ}{.}9$ for component N1 to $\theta_{\rm var} = 1\overset{\circ}{.}2$ for N4, which travels almost directly along the line of sight. This change in the jet orientation is readily apparent when analyzing each component's position angle shortly after the time of ejection, as well as their subsequent trajectories, as shown in Figure 9.

This smaller viewing angle of the jet with respect to the observer during the second radio flare, which appears to last until the end of our VLBA data set (2014 June), is also in agreement with the significant differences observed between the ejections of components N1 and N4. While component N1 is clearly identified in the jet as a bright ($\gtrsim$2 Jy) component soon after its ejection, most of the increase in the total flux density during the second radio flare appears to be associated with the core region (C0+C1), with component N4 representing only a small fraction of the flare. The smaller viewing angle of the jet also leads to a more difficult identification of component N4, which is not clearly discerned from the core until 2014 May (2014.33). Further support for the re-orientation of the jet toward the observed is also obtained from the analysis of the polarization, discussed in Section 6.

## 5. CROSS-CORRELATION ANALYSIS

To quantify the relationship among the light curves at the different wavebands, we perform a discrete cross-correlation analysis. The $z$-transformed discrete correlation function (ZDCF) described by Alexander (1997) has been designed for unevenly sampled light curves, as in our case. We use the publicly available *zdcf_v1.2* and *plike_v4.0.f90* programs,[22] with a minimum number of 11 points inside each bin, as recommended for a meaningful statistical interpretation. We compute the DCF between each pair of light curves, including data from 100 days before to 100 days after the main $\gamma$-ray outburst. Time sampling of the light curves ranges from one day for the $\gamma$-ray data to tens of days in the case of some other wavebands (see Figure 2).

Figure 10 displays the ZDCF analysis for the optical-$\gamma$ (upper panel) and UV-$\gamma$ (lower panel) data. We find that the correlation peaks between the $\gamma$-ray light curve and the optical and UV light curves give a time lag of 0.70 ± 1 and $1.23^{+5.00}_{-4.09}$ days, respectively, where a positive lag means that the $\gamma$-ray variations lead. We therefore conclude that the variations at the three wavelengths are essentially coincident within the uncertainties.

The sparser sampling of the X-ray data, as well as its double-peaked structure, precludes a reliable ZDCF analysis. However, we note that the first X-ray data peak is coincident with the $\gamma$-ray flare, and the second brighter X-ray flare occurs ∼50 days later (see Figure 2). The triple-flare structure of the NIR light curve during the $\gamma$-ray flare (see Figure 3) also prevents a unique interpretation of a cross-correlation analysis. Nevertheless, from inspection of the light curves, we see that the first, brightest peak in the NIR light curve (56193 MJD) is simultaneous with the $\gamma$-ray outburst within an uncertainty of one day, corresponding to the time sampling of both light curves.

We obtain no significant correlation between the millimeter-wave and $\gamma$-ray light curves. This can be due to the different timescales associated with the emission at these wavebands, as also suggested for other blazars (e.g., 1156+295; Ramakrishnan et al. 2014). The rise time for the millimeter-wave band is of the order of months, while for the $\gamma$-rays it is of the order of a few days. We note, however, that the 1, 3, and 7 mm light curves contain a significant flare coincident with the $\gamma$-ray outburst.

## 6. POLARIZED EMISSION

Figure 11 shows the optical and millimeter-wave linear polarization between MJD 54000 and 56900, covering the period of the $\gamma$-ray flare. To solve for the $\pm n\pi$ ambiguity in the EVPA, we assume the slowest possible variation in time, applying a $\pm\pi$ rotation between two consecutive measurements when the magnitude of the EVPA change would otherwise exceed $\pi/2$.

No significant increase in the degree of polarization at millimeter wavelengths is observed during the $\gamma$-ray flare, but the EVPAs display a progressive rotation starting about one year prior to the $\gamma$-ray flare. Figure 11 shows that between 2007 and mid-2011 the EVPAs at 3 and 1 mm are distributed around a mean value of ∼100°. After this, the polarization at millimeter wavelengths starts a slow rotation by almost 80° in one year (from 2011 July to 2012 August) until the flare epoch. In coincidence with the $\gamma$-ray flare, the rate of EVPA rotation in the VLBI core and stationary component C1 increases significantly, leading to a rotation of almost 200° in one year. Subsequently, component N4 appears and the EVPAs of both C1 and N4 rotate again toward values similar to those at 1 and 3 mm, reaching ∼−100°. It is possible that during the flare, while the new superluminal component N4 is crossing the core zone, the EVPAs of the innermost region at 7 mm rotate due to the passage of the component. After this, when N4 can be distinguished from C1 and C0, the EVPAs at 7 mm again follow the general behavior of the EVPAs at shorter millimeter wavelengths. A similar discrepancy between the 1–3 and 7 mm EVPAs occurs between mid-2009 and mid-2010, when

[22] http://www.weizmann.ac.il/weizsites/tal/research/software/

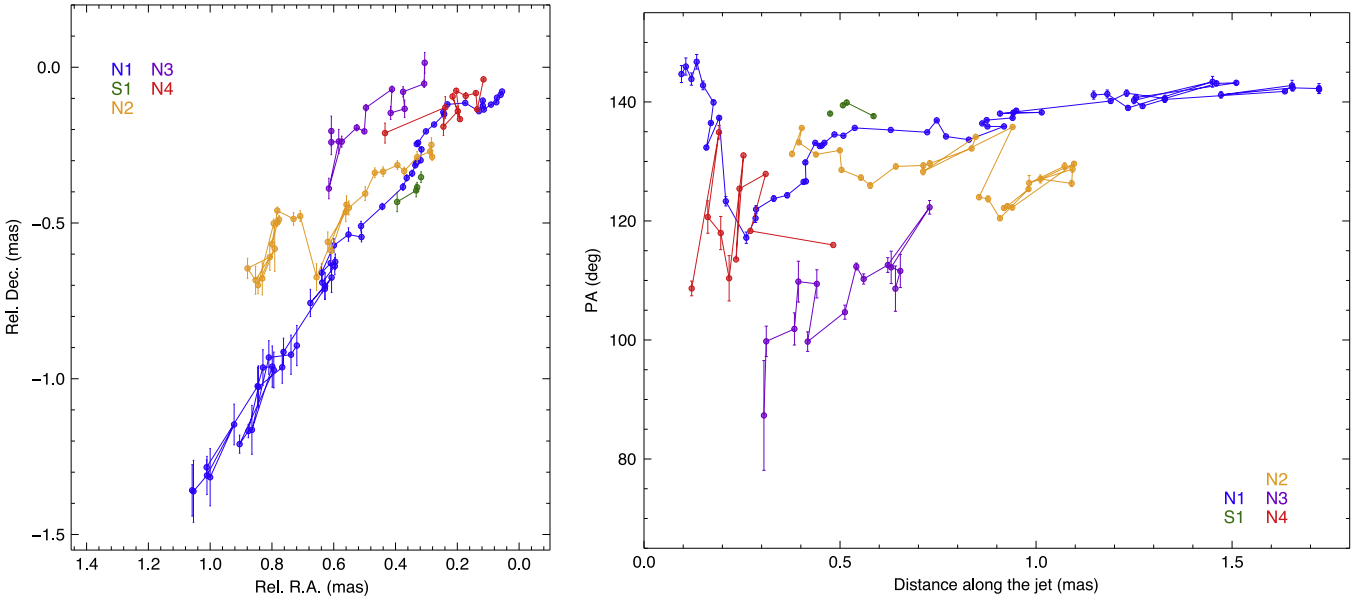


**Figure 9.** Trajectories (left panel) and position angles as a function of distance from the core (right panel) of the moving components in the jet.

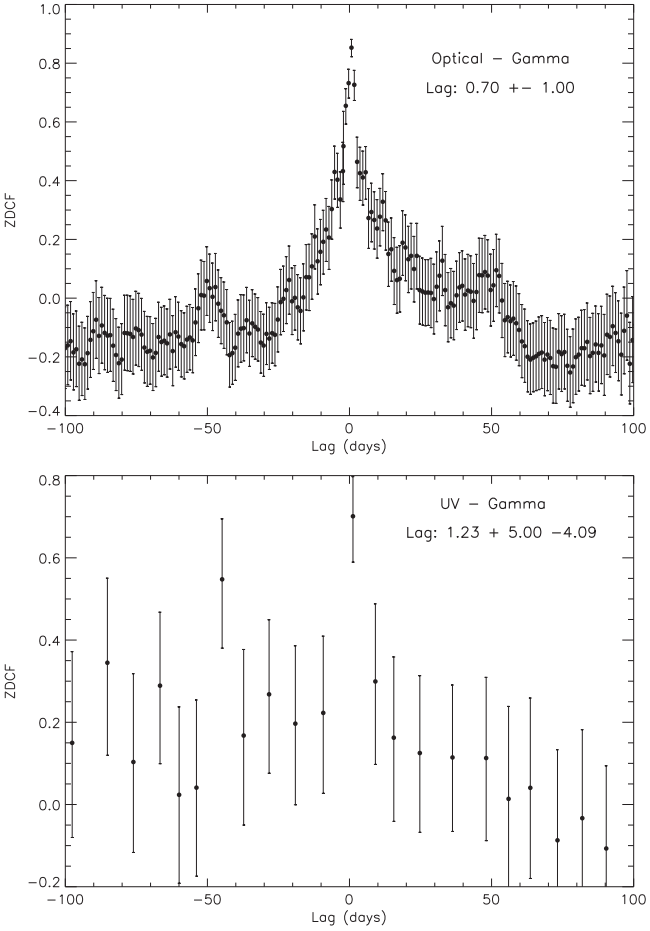


**Figure 10.** *Z*-transformed discrete correlation function between optical and $\gamma$-ray data (upper panel) and UV and $\gamma$-ray data (lower panel). In each panel, we report the time lag corresponding to the correlation peak with its respective $1\sigma$ error (see Alexander 2013 for more details).

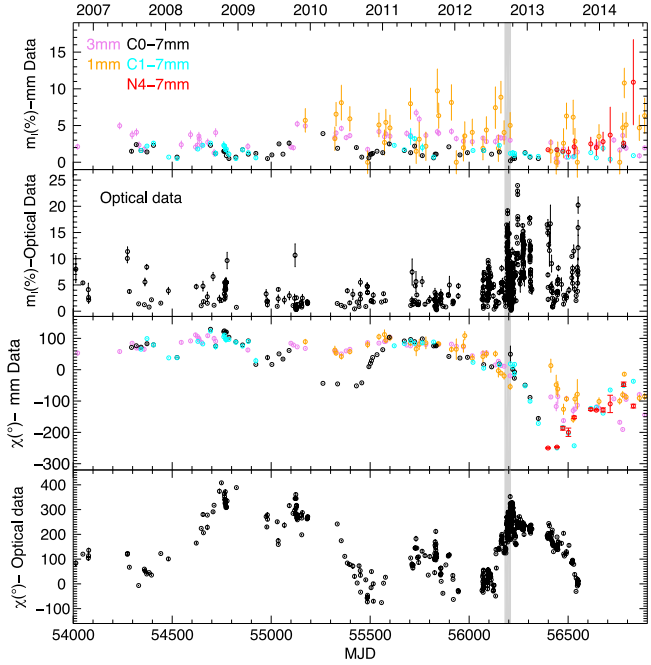


**Figure 11.** Optical and millimeter-wave linear polarization over the period MJD 54000–56800. The first two panels display the degree of millimeter-wave and optical polarization, respectively. The third and fourth panels display the EVPAs at millimeter and optical wavelengths, respectively. The gray vertical stripe indicates the epoch of the main $\gamma$-ray flare.

component N1 is ejected and becomes brighter than the core until mid-2010 (see Figure 8).

We can then distinguish the rapid rotation of polarization vectors observed in the VLBI components at 7 mm after the flare from the slower rotation observed at 1 and 3 mm. The latter leads to a rotation of the mm-EVPAs of $\sim$200° over 3 years (from 2011 July to 2014 August). This progressive

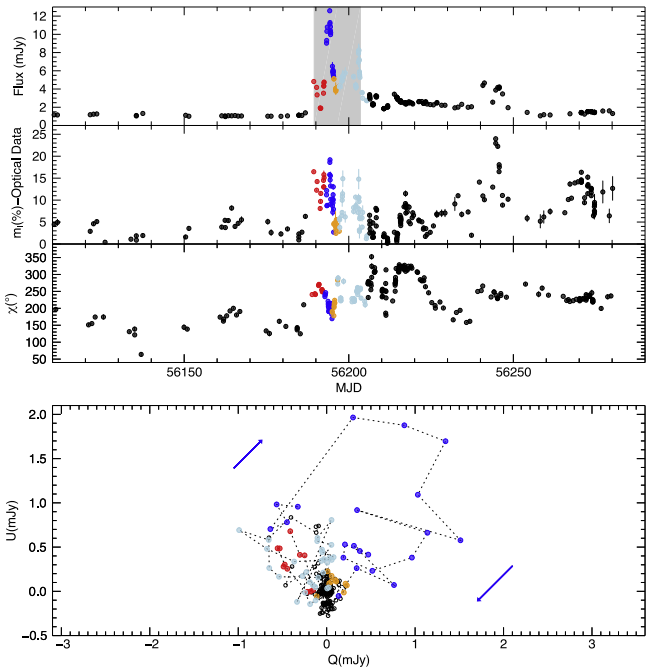


**Figure 12.** Upper panel displays, from top to bottom, the light curve, degree and time evolution of polarization, and EVPA at optical frequencies. Each colored mark corresponds to the period over which we plot the $U$ and $Q$ Stokes parameters in the lower panel. Blue points mark a clockwise rotation cycle that occurs in coincidence with the total intensity peak. The gray vertical stripe indicates the time range of the main gamma-ray flare.

rotation in the EVPAs can be produced by a change in the orientation of the innermost jet, which would be in agreement with the larger Doppler factor and smaller viewing angle of component N4 associated with the $\gamma$-ray event, as discussed previously (see Section 4).

The optical polarization executes rapid and pronounced changes in both degree of polarization and EVPA associated with the $\gamma$-ray flare. Figure 12 displays an expanded view of the optical polarization data near the time of the $\gamma$-ray flare, with four different time ranges marked in different colors. Before the peak at optical frequencies on MJD 56194, the source undergoes a period of rapid changes in both total and polarized emission (marked in red), and the EVPAs rotate by almost 30°. The plot of Stokes parameters $U$ versus $Q$ in Figure 12 reveals a clear clockwise rotation of the EVPAs (marked in blue), in coincidence with the main flare in total flux and a rapid change in the degree of polarization. This clockwise rotation has been previously reported by Larionov et al. (2013a).

If we assume a model in which a relativistic shock does not cover the entire cross-section of the jet and is moving down the jet following helical magnetic field lines, which also propagate downstream, then we expect to observe a rotation in the EVPA. This should be accompanied by a change in the degree of polarization, with a minimum in the middle of the rotation, where the flaring region contains magnetic field lines with opposite polarity (e.g., Vlahakis 2006; Marscher et al. 2008; Larionov et al. 2013b). Evidence of a helical magnetic field in CTA 102 jet can also be found in the detection of negative circular polarization (Gabuzda et al. 2008) and in a gradient in the rotation measure across the jet width at about 7 mas from the core (Hovatta et al. 2012), both in MOJAVE observations.

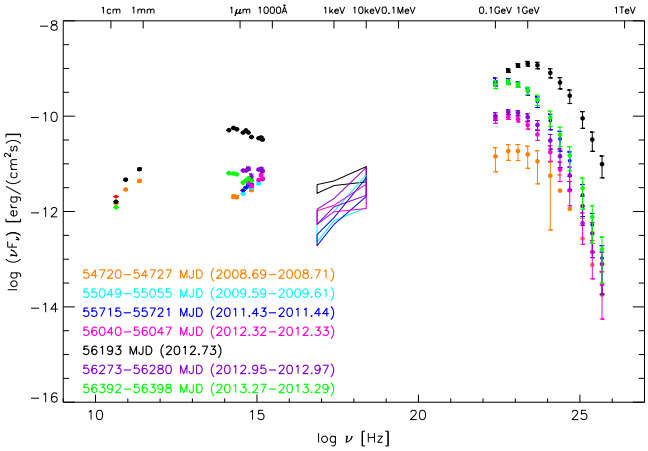


**Figure 13.** Spectral energy distribution of CTA 102 from millimeter-wave to $\gamma$-ray frequencies during the brightest $\gamma$-ray flare (black) and at other observing epochs, as labeled in the figure and discussed in the text.

## 7. SPECTRAL ENERGY DISTRIBUTION

We have computed the spectral energy distribution (SED) of the source from millimeter to $\gamma$-ray wavelengths at several epochs (see Figure 13): two epochs between MJD 54720 and MJD 55055, corresponding to $\gamma$-ray quiescent states; the epochs of the first $\gamma$-ray flare (MJD 55715–55721), the main flare (MJD 56193), and the third $\gamma$-ray flare (MJD 56392–56398); one epoch of a quiescent state between the first and second flares (MJD 56040–56047), and a second one between the second and third flares (MJD 56273–56280). For the main $\gamma$-ray flare, all data are simultaneous except for the millimeter-wave data, which corresponds to MJD 56208. For the other epochs, we have considered a range of time (as indicated in Figure 13) in order to cover the entire energy range.

By examining Figure 13, we observe that, during the multi-wavelength flare in 2012 (black points), both the synchrotron and the inverse-Compton peaks increased. The synchrotron peak frequency during the flare is close to $10^{14}$ Hz, at the upper end of the frequency range $10^{12}$–$10^{14}$ Hz of synchrotron peaks observed in luminous blazars (Ghisellini & Tavecchio 2008). At the same time, we also observe a shift in the inverse-Compton peak to higher frequencies, which leads to a hardening of the spectrum between 0.1 and 1 GeV. We note that neither of the other two, weaker $\gamma$-ray flares displays a similar shift in the peak of the inverse-Compton spectrum. In particular, the weaker first and third $\gamma$-ray flares display a very similar inverse-Compton spectrum, peaking at nearly the same frequency, with only a minor hardening toward higher energies during the third flare. The shift of the $\gamma$-ray peak toward higher frequencies during the main $\gamma$-ray flare can be explained by a change in the viewing angle—leading to an increase in Doppler factor—of the emitting region, in support of our hypothesis of a reorientation of the jet toward the line of sight during the multi-wavelength flare (see Sections 4 and 6).

The ratio of the inverse-Compton to synchrotron peaks is of the order of 10, which is not sufficiently large to rule out synchrotron self-Compton (SSC) scattering as the main mechanism for the production of the $\gamma$-ray emission (e.g., Sikora et al. 2009).

## 8. DISCUSSION AND RESULTS

We have presented a multi-wavelength polarimetric study of the quasar CTA 102 during an unprecedented $\gamma$-ray outburst that was observed between 2012 September 23 and October 2. We find that the $\gamma$-ray outburst occurred simultaneously with flares from millimeter to X-ray wavelengths, with the exception that the 1 and 7 mm light curves peak almost one month after the shorter-wavelength flares. However, all of the millimeter-wave light curves begin to increase before the shorter-wavelength outburst, but took longer times to reach maximum flux and then to decay.

Our DCF analysis confirms the coincidence between the $\gamma$-ray flare and the optical-UV flare. The same analysis does not provide unambiguous correlation between the X-ray or NIR and the $\gamma$-ray light curves because of the multi-peak structure of the flare at these two frequencies and the relatively sparse sampling.

The *Fermi* LAT daily light curve reveals two more $\gamma$-ray outbursts apart from that in 2012: one in 2011 June and the other in 2013 April. Both outbursts are weaker and "orphan." Only the bright outburst in 2012 September–October is coincident with flares at the other wavelengths and with the emergence of a new superluminal knot from the radio core.

We have combined our multi-wavelength study of light curves with an analysis of multi-epoch VLBA observations at 43 GHz that provide the necessary angular resolution to follow the evolution of the jet during the outburst. In the 43 GHz VLBA images, we observe the ejection of multiple superluminal knots from the radio core during the analyzed period, but only one of these knots, N4, is associated with a $\gamma$-ray flare. Component N4 was ejected in 2012.49 $\pm$ 0.11, within a time range between 47 and 127 days before the main $\gamma$-ray flare in 2012 (2012.73), when the radio core started to increase in flux density. The interaction between a traveling feature and the stationary radio core appears to have triggered a number of $\gamma$-ray outbursts in blazars (e.g., Morozova et al. 2014; Ramakrishnan et al. 2014) and radio galaxies (Grandi et al. 2012; Casadio et al. 2015). However, not every ejection of a new knot leads to a $\gamma$-ray flare. For instance, it is not clear why a $\gamma$-ray flare is associated with N4 in CTA 102 and not with the other moving radio components.

From the analysis of model-fit components at 43 GHz, we deduce that the jet changed its orientation with respect to the observer when component N4 was ejected. This is derived from an analysis of the variability Doppler factor and viewing angle, which indicates that a progressive increase in the Doppler factor occurred, caused by a re-orientation of the jet toward the line of sight. This led to a minimum viewing angle of $\theta \sim 1\overset{\circ}{.}2$ when component N4 was ejected during the $\gamma$-ray outburst. This change in the orientation of the jet is supported by the observed progressive, slow rotation of the millimeter-wave EVPAs starting almost one year before the ejection of N4 and the $\gamma$-ray flare. We therefore conclude that the $\gamma$-ray emission in CTA 102 is related to a decrease in the viewing angle of the jet.

This correlation between $\gamma$-ray activity and orientation of the jet has been already observed in other BL Lac objects (Marscher et al. 2008; Larionov et al. 2010; Rani et al. 2014), quasars (Abdo et al. 2010b; Raiteri et al. 2011; Jorstad et al. 2013), and radio galaxies (Casadio et al. 2015), although there are different interpretations regarding the cause of the change in orientation. Some authors consider a bent or precessing jet, while others suggest a helical jet with the radiating component following this helical path. A helical trajectory could also be the consequence of magnetic field lines twisting around a conical or parabolic jet (Vlahakis 2006).

In the case of CTA 102, there are indications of a helical magnetic field structure (Gabuzda et al. 2008; Hovatta et al. 2012). We associate the fast variability in the polarized optical emission, as well as the clockwise rotation displayed in the EVPAs during the outburst, with the helical path followed by the superluminal component in its motion along the outwardly propagating magnetic field lines. On the other hand, a number of similar rotations of the millimeter-wave and optical polarization vectors occurred in both the clockwise and counterclockwise directions over the entire 2004–2014 monitoring period. This can be interpreted in terms of random walks of a turbulent magnetic field (Jones 1988; D'Arcangelo et al. 2007; Marscher 2014). Early results from the RoboPol program show that, while many EVPA rotations related to $\gamma$-ray flares can be produced by a random walk process, some are not (Blinov et al. 2015). If the rotation associated with a $\gamma$-ray flare is caused by a helical geometry of the magnetic field, then future such outbursts should be accompanied by similar clockwise rotations.

The observed long-term rotation in millimeter-wave polarization vectors, together with the slower proper motion associated with component N4, suggests a change in the jet orientation, so that it becomes more closely aligned with the line of sight during the ejection of component N4 and the multi-wavelength flare.

The close timing of the $\gamma$-ray, X-ray, UV, and optical flares suggests co-spatiality of the emission at all these frequencies. Knot N4 was 0.025–0.07 mas downstream of the core when the $\gamma$-ray flare occurred, i.e., it had not yet reached the feature C1 at $\sim$0.1 mas. This is confirmed by the increase in flux density in the 7 mm core during the $\gamma$-ray outburst. Hence, we conclude that the bright $\gamma$-ray outburst occurred inside the millimeter-wave core region.

We observe component N4 for the first time in the VLBA images on 2013 April (MJD 56398), when it was located at $r \sim$ 0.12 mas. The $\gamma$-ray flare in 2013 April occurred between MJD 56387 and 56394. Therefore, a possible interpretation of this flare is the passage of component N4 through C1, interpreted by Fromm et al. (2013a) as a possible recollimation shock.

If the radio core were located within $\sim$1 pc of the black hole (BH), then the accretion disk or the broad-line region could provide the necessary photon field to explain the high-energy emission through external Compton scattering. The 43 GHz radio core in CTA 102 must be coincident with, or downstream of, the 86 GHz core that is located at a distance of 7.5 $\pm$ 3.2 pc ($\sim 8.5 \times 10^4$ gravitational radii for a BH mass of $\sim 8.5 \times 10^8 M_\odot$; Zamaninasab et al. 2014) from the BH (Fromm et al. 2015). A similar scaled distance, $\sim 10^4$–$10^5$ gravitational radii, has been determined also for two radio galaxies, 3C 111 and 3C 120 (Marscher et al. 2002; Chatterjee et al. 2009, 2011) and two blazars, BL Lac and 3C 279 (Marscher et al. 2008; Abdo et al. 2010b). For a mean viewing angle of the jet of CTA 102 of $2\overset{\circ}{.}6$ (Jorstad et al. 2005; Fromm et al. 2015), the distance of N4 from C0 is 4.6–13 pc, hence the $\gamma$-ray outburst took place more than 12 pc from the BH. At this location, there should be a negligible contribution of photons from the disk or the broad-line region, or from the dusty torus (located $\sim$1.6 pc from the BH; Pacciani et al. 2014), for

external Compton scattering to produce the high-energy flare. The lack of a suitably strong external source of photons favors SSC scattering of NIR to UV photons by electrons in the jet with energies ∼10 times the rest-mass energy as the source of the γ-ray emission. The ratio of γ-ray to infrared (synchrotron) luminosity is $\lesssim$10, sufficiently low to be consistent with the SSC process.

## 9. CONCLUSION

Our study of the time variability of the multi-wavelength flux and linear polarization of the quasar CTA 102 confirms its erratic blazar nature, revealing both strong connections across wavebands in one outburst and no obvious connections for other events. The bright γ-ray outburst in late 2012 was accompanied by contemporaneous flares at longer wavelengths up to at least 8 mm, with the increase in millimeter-wave flux starting before the γ-ray activity. The polarization vector at both optical and millimeter wavelengths rotated from the time of the γ-ray peak until ∼150 days later. A new superluminally moving knot, N4—the feature with the highest Doppler beaming factor during our monitoring, according to our analysis—was coincident with the core in the 43 GHz VLBA images 47–127 days prior to the γ-ray peak. We conclude that the outburst was so luminous because the jet (or, at least, the portion of the jet where most of the emission occurs) had shifted to a direction closer to the line of sight than was previously the case. The time delay between the epoch when N4 crossed the centroid of the core (feature C0) and the epoch of peak γ-ray emission implies that the main flare took place $\gtrsim$12 pc from the BH. At this distance, the only plausible source of seed photons for inverse-Compton scattering is NIR to UV emission from the jet itself. The ratio of γ-ray to infrared luminosity is only ∼10 at the peak of the outburst, low enough to be consistent with SSC high-energy emission.

Multiple superluminal knots appeared in the jet during the 7 years covered by our VLBA observations. These include a very bright component (N1) ejected in $2009.12 \pm 0.02$ and associated with a significant millimeter-wave flare in the core region (∼4.2 Jy). Yet, only component N4 is related to a flare at γ-ray energies. Two strong "orphan" γ-ray flares have no apparent optical counterparts. A strong millimeter-wave event with neither a γ-ray nor optical counterpart can be explained by an inability of the event to accelerate electrons up to energies $\sim 10^4 mc^2$ needed to radiate at such frequencies, although the reason for this inability is unclear. Orphan γ-ray flares might be explained by a knot crossing a region where there is a higher local density of seed photons for inverse-Compton scattering (Marscher et al. 2010; MacDonald et al. 2015). Indeed, the second orphan flare corresponds to the time of passage of knot N4 through stationary feature C1 (located ∼0.1 mas from the core), which could be such a region.

During the multi-wavelength outburst we observe intra-day variability in the optical polarized emission, as well as a clockwise rotation in optical EVPAs. This rotation could be caused by a spiral path traced by the knot moving along helical magnetic field lines that propagate outwards relativistically. Alternatively, the various rotations of the polarization vector seen in our data set, which are in the clockwise and counterclockwise direction over different time ranges, could be mainly random walks caused by a turbulent magnetic field.

CTA 102 displays the complex behavior characteristic of the blazar class of active galactic nuclei. Nevertheless, we have found possible connections between variations in the multi-wavelength flux and polarization and in the structure of the jet in some events. Continued monitoring of CTA 102 and other bright blazars at multiple wavebands with as dense a sampling as possible, combined with millimeter-wave VLBI imaging, can eventually determine which connections are robust and the extent to which stochastic processes dominate the behavior of blazars.

This research has been supported by the Spanish Ministry of Economy and Competitiveness (MINECO) grant AYA2013-40825-P. The research at Boston University (BU) was funded in part by NASA Fermi Guest Investigator grants NNX14AQ58G and NNX13AO99G, and Swift Guest Investigator grant NNX14AI96G. I.A. acknowledges support by a Ramón y Cajal grant of the MINECO. The VLBA is operated by the National Radio Astronomy Observatory. The National Radio Astronomy Observatory is a facility of the National Science Foundation operated under cooperative agreement by Associated Universities, Inc. The PRISM camera at Lowell Observatory was developed by K. Janes et al. at BU and Lowell Observatory, with funding from the NSF, BU, and Lowell Observatory. St. Petersburg University team acknowledges support from Russian RFBR grant 15-02-00949 and St. Petersburg University research grant 6.38.335.2015. This research was conducted in part using the Mimir instrument, jointly developed at Boston University and Lowell Observatory and supported by NASA, NSF, and the W.M. Keck Foundation. The Mimir observations were performed by Lauren Cashman, Jordan Montgomery, and Dan Clemens, all from Boston University. This research is partly based on data taken at the IRAM 30 m Telescope. IRAM is supported by INSU/CNRS (France), MPG (Germany), and IGN (Spain). The Submillimeter Array is a joint project between the Smithsonian Astrophysical Observatory and the Academia Sinica Institute of Astronomy and Astrophysics and is funded by the Smithsonian Institution and the Academia Sinica. Data from the Steward Observatory spectropolarimetric monitoring project were used. This program is supported by Fermi Guest Investigator grants NNX08AW56G, NNX09AU10G, and NNX12AO93G. The Metsähovi team acknowledges the support from the Academy of Finland to our observing projects (numbers 212656, 210338, 121148, and others).

## REFERENCES

Abdo, A. A., Ackermann, M., Ajello, M., et al. 2010a, ApJ, 715, 429
Abdo, A. A., Ackermann, M., Ajello, M., et al. 2010b, Natur, 463, 919
Ackermann, M., Ajello, M., Allafort, A., et al. 2011, ApJ, 743, 171
Agudo, I., Gómez, J.-L, Marti, J.-M., et al. 2011, ApJL, 549, L183
Agudo, I., Krichbaum, T. P., Ungerechts, H., et al. 2006, A&A, 456, 117
Agudo, I., Molina, S. N., Gómez, J. L., et al. 2012, IJMPS, 8, 299
Agudo, I., Thum, C., Gómez, J. L., & Wiesemeyer, H. 2014, A&A, 566, A59
Agudo, I., Thum, C., Wiesemeyer, H., & Krichbaum, T. P. 2010, ApJS, 189, 1
Alexander, T. 1997, in Astrophysics and Space Science Library 218, Astronomical Time Series, ed. D. Maoz, A. Sternberg & E. M. Leibowitz (Dordrecht: Kluwer), 163
Alexander, T. 2013, arXiv:1302.1508
Blinov, D., Pavlidou, V., Papadakis, I., et al. 2015, MNRAS, 453, 1669
Burbidge, G. R., Jones, T. W., & Odell, S. L. 1974, ApJ, 193, 43
Cardelli, J. A., Clayton, G. C., & Mathis, J. S. 1989, ApJ, 345, 245
Carrasco, L., Luna, A., Porras, A., & Mayya, D. Y. 2012, ATel, 4442, 1
Casadio, C., Gómez, J. L., Grandi, P., et al. 2015, ApJ, 808, 162
Chatterjee, R., Marscher, A. P., Jorstad, S. G., et al. 2009, ApJ, 704, 1689
Chatterjee, R., Marscher, A. P., Jorstad, S. G., et al. 2011, ApJ, 734, 43
Clemens, D. P., Sarcia, D., Grabau, A., et al. 2007, PASP, 119, 1385

D'Arcangelo, F. D., Marscher, A. P., Jorstad, S. G., et al. 2007, ApJL, 659, L107
Fromm, C. M., Perucho, M., Ros, E., Savolainen, T., & Zensus, J. A. 2015, A&A, 576, A43
Fromm, C. M., Perucho, M., Ros, E., et al. 2011, A&A, 531, A95
Fromm, C. M., Ros, E., Perucho, M., et al. 2013a, A&A, 551, A32
Fromm, C. M., Ros, E., Perucho, M., et al. 2013b, A&A, 557, A105
Gabuzda, D. C., Vitrishchak, V. M., Mahmud, M., & O'Sullivan, S. P. 2008, MNRAS, 384, 1003
Ghisellini, G., & Tavecchio, F. 2008, MNRAS, 387, 1669
Gómez, J.-L., Marscher, A. P., Alberdi, A., Jorstad, S. G., & Agudo, I. 2001, ApJL, 561, L161
Gómez, J., Marscher, A., Alberdi, A., et al. 2002, Polarization Calibration of the VLBA Using the D-terms, Tech. Rep., National Radio Astronomy Observatory, VLBA Scientific Memo
Grandi, P., Torresi, E., & Stanghellini, C. 2012, ApJL, 751, L3
Gurwell, M. A., Peck, A. B., Hostler, S. R., Darrah, M. R., & Katz, C. A. 2007, in ASP Conf. Ser. 375, From Z-Machines to ALMA: (Sub) Millimeter Spectroscopy of Galaxies, ed. A. J. Baker et al. (San Francisco, CA: ASP), 234
Hagen-Thorn, V. A., Larionov, V. M., Jorstad, S. G., et al. 2008, ApJ, 672, 40
Hovatta, T., Lister, M. L., Aller, M. F., et al. 2012, AJ, 144, 105
Hovatta, T., Valtaoja, E., Tornikoski, M., & Lähteenmäki, A. 2009, A&A, 494, 527
Itoh, R., Fukazawa, Y., Tanaka, Y. T., et al. 2013, ApJL, 768, L24
Jones, T. W. 1988, ApJ, 332, 678
Jorstad, S. G., Marscher, A. P., Larionov, V. M., et al. 2010, ApJ, 715, 362
Jorstad, S. G., Marscher, A. P., Lister, M. L., et al. 2005, AJ, 130, 1418
Jorstad, S. G., Marscher, A. P., Mattox, J. R., et al. 2001, ApJS, 134, 181
Jorstad, S. G., Marscher, A. P., Smith, P. S., et al. 2013, ApJ, 773, 147
Larionov, V., Blinov, D., & Jorstad, S. 2012, ATel, 4397, 1
Larionov, V. M., Blinov, D. A., Jorstad, S. G., et al. 2013a, EPJWC, 61, 4019
Larionov, V. M., Jorstad, S. G., Marscher, A. P., et al. 2013b, ApJ, 768, 40
Larionov, V. M., Villata, M., & Raiteri, C. M. 2010, A&A, 510, A93
Lister, M. L., Aller, M. F., Aller, H. D., et al. 2013, AJ, 146, 120
Lister, M. L., Cohen, M. H., Homan, D. C., et al. 2009, AJ, 138, 1874
MacDonald, N. R., Marscher, A. P., Jorstad, S. G., & Joshi, M. 2015, ApJ, 804, 111
Maraschi, L., Ghisellini, G., Tanzi, E. G., & Treves, A. 1986, ApJ, 310, 325
Marscher, A. P. 2014, ApJ, 780, 87
Marscher, A. P., Jorstad, S. G., D'Arcangelo, F. D., et al. 2008, Natur, 452, 966
Marscher, A. P., Jorstad, S. G., Gómez, J.-L., et al. 2002, Natur, 417, 625
Marscher, A. P., Jorstad, S. G., Larionov, V. M., et al. 2010, ApJL, 710, L126
Mead, A. R. G., Ballard, K. R., Brand, P. W. J. L., et al. 1990, A&AS, 83, 183
Moore, R. L., & Stockman, H. S. 1981, ApJ, 243, 60
Morozova, D. A., Larionov, V. M., Troitsky, I. S., et al. 2014, AJ, 148, 42
Nolan, P. L., Abdo, A. A., Ackermann, M., et al. 2012, ApJS, 199, 31
Osterman Meyer, A., Miller, H. R., Marshall, K., et al. 2009, AJ, 138, 1902
Pacciani, L., Tavecchio, F., Donnarumma, I., et al. 2014, ApJ, 790, 45
Pica, A. J., Smith, A. G., Webb, J. R., et al. 1988, AJ, 96, 1215
Planck Collaboration, Ade, P. A. R., Aghanim, N., et al. 2014, A&A, 571, A16
Poole, T. S., Breeveld, A. A., Page, M. J., et al. 2008, MNRAS, 383, 627
Raiteri, C. M., Villata, M., Aller, M. F., et al. 2011, A&A, 534, A87
Ramakrishnan, V., León-Tavares, J., Rastorgueva-Foi, E. A., et al. 2014, MNRAS, 445, 1636
Rani, B., Krichbaum, T. P., Marscher, A. P., et al. 2014, A&A, 571, L2
Rantakyrö, F. T., Wiik, K., Tornikoski, M., Valtaoja, E., & Bååth, L. B. 2003, A&A, 405, 473
Savolainen, T., Wiik, K., Valtaoja, E., Jorstad, S. G., & Marscher, A. P. 2002, A&A, 394, 851
Schlafly, E. F., & Finkbeiner, D. P. 2011, ApJ, 737, 103
Schmidt, G. D., Stockman, H. S., & Smith, P. S. 1992, ApJL, 398, L57
Sikora, M., Stawarz, Ł., Moderski, R., Nalewajko, K., & Madejski, G. M. 2009, ApJ, 704, 38
Smith, P. S., Montiel, E., Rightley, S., et al. 2009, arXiv:0912.3621
Spencer, R. E., McDowell, J. C., Charlesworth, M., et al. 1989, MNRAS, 240, 657
Stanghellini, C., O'Dea, C. P., Dallacasa, D., et al. 1998, A&A, 131, 303
Vlahakis, N. 2006, in ASP Conf. Ser. 350, Blazar Variability Workshop II: Entering the GLAST Era, ed. H. R. Miller et al. (San Francisco, CA: ASP), 169
Williamson, K. E., Jorstad, S. G., Marscher, A. P., et al. 2014, ApJ, 789, 135
Zamaninasab, M., Clausen-Brown, E., Savolainen, T., & Tchekhovskoy, A. 2014, Natur, 510, 126
Zensus, J. A., Ros, E., Kellermann, K. I., et al. 2002, AJ, 124, 662